symmetry

IMPACT FACTOR 2.2

CITESCORE 5.3

Article

Distinguishing Strongly Interacting Dark Matter Spikes via EMRI Gravitational Waves

Yu Wang, Rundong Tang, Wenbiao Han and Enwei Liang

MDPI

https://doi.org/10.3390/sym17111878

symmetry

MDPI

Article

Distinguishing Strongly Interacting Dark Matter Spikes via EMRI Gravitational Waves

Yu Wang [1,2,*], Rundong Tang [2], Wenbiao Han [2] and Enwei Liang [1]

[1] School of Physical Science and Technology, Guangxi University, Nanning 530004, China; lew@gxu.edu.cn
[2] Shanghai Astronomical Observatory, Chinese Academy of Sciences, Shanghai 200030, China; trd@shao.ac.cn (R.T.); wbhan@shao.ac.cn (W.H.)
* Correspondence: 2107401023@st.gxu.edu.cn

Abstract

We investigate the potential of extreme mass ratio inspirals (EMRIs) as probes of strongly interacting dark matter (SIDM) spikes around supermassive black holes. Based on Lagrangian formulations of dark matter self-interactions, we analyze the effects of number changing processes, such as $2 \to 0$ annihilation and $3 \to 2$ scattering, on the inner density profiles, and propose a generalized definition of the dissolution radius, including its dependence on the central black hole mass. Building on this framework, we construct dark matter spike models suitable for phase shift calculations and study the gravitational waves of EMRIs under the circular orbit adiabatic approximation. Our analysis shows that different interaction mechanisms produce distinct dark matter density distributions, resulting in characteristic phase differences in the gravitational waveforms. The magnitudes of these phase shifts are well above the resolution threshold of space-based detectors. We conclude that future missions, such as *LISA*, will be able to distinguish different SIDM interaction channels through precise waveform measurements, thereby opening a new avenue for probing the microphysics of dark matter in extreme astrophysical environments.

Keywords: dark matter; spike; gravitational waves

Received: 10 September 2025
Revised: 9 October 2025
Accepted: 11 October 2025
Published: 5 November 2025

Citation: Wang, Y.; Tang, R.; Han, W.; Liang, E. Distinguishing Strongly Interacting Dark Matter Spikes via EMRI Gravitational Waves. *Symmetry* **2025**, *17*, 1878. https://doi.org/10.3390/sym17111878

1. Introduction

Unraveling the true nature of dark matter (DM) remains one of the greatest challenges in contemporary astrophysics and cosmology. Although the cold and collisionless dark matter (CDM) paradigm has achieved remarkable success in accounting for large-scale structure formation—explaining observations such as cosmic microwave background anisotropies, galaxy clustering, and the evolution of the cosmic web—persistent discrepancies at galactic and sub-galactic scales have prompted the investigation of alternative scenarios. Noteworthy examples include the core–cusp problem, the missing satellites problem, and the too-big-to-fail problem [1]. These unresolved tensions indicate that the CDM framework may not fully capture the complexity of dark matter on small scales, particularly within dense environments.

Among the various proposed solutions, strongly interacting dark matter (SIDM) has emerged as a compelling extension, in which DM particles experience elastic scatterings with appreciable cross sections. Such interactions can redistribute energy and yield cored density profiles in the central regions of galaxies [2]. Furthermore, number changing processes—such as semi-annihilation and $3 \to 2$ interactions—featured in Strongly Interacting Massive Particle (SIMP) models, provide alternative thermal freeze-out mechanisms and

can profoundly affect the thermal evolution and structure of DM halos [3,4]. These interactions can inject energy into dense regions, thereby altering or even erasing the anticipated central spikes.

The regions surrounding SMBH offer a particularly sensitive environment for probing the microphysics of DM. In the conventional CDM framework, gravitational contraction can produce pronounced DM spikes with steep power-law density profiles [5]. However, these spikes are fragile and may be significantly altered or even destroyed by DM self-interactions and number changing processes, leading to substantial changes in the central density structure [6,7]. Recent advancements in axion dark matter research, such as those by Gao et al. (2025) [8], highlight the role of ALPs in forming dense structures around black holes through self-interactions and condensate dynamics. Incorporating these insights could further illuminate the microphysical mechanisms underlying spike formation. Furthermore, theoretical studies have explored related microphysical mechanisms, including dark photons and tachyonic instabilities induced by the Barbero–Immirzi parameter and axion–torsion transmutation, which could also influence the dynamics of dense dark matter structures around compact objects [9]. In addition, recent theoretical developments have investigated the possible role of quantum corrections and torsional gravity effects, suggesting that chiral dark dynamos induced by the Barbero–Immirzi field and Nieh–Yan gravity could impact the evolution of dark sectors in the early universe [10]. Earlier investigations have also examined fermionic field dynamics in curved and rotating spacetimes. In particular, Gao et al. studied the scattering of Dirac spinors in rotating spheroidal geometries, demonstrating how spin–rotation coupling and geometric deformation affect the propagation of quantum fields in strong gravitational backgrounds [11]. Such analyses provide useful theoretical context for understanding the microphysical behavior of fermionic or axion-like dark matter near compact objects. Another relevant development involves modified gravity theories, such as the ghost-free Gauss–Bonnet extensions of general relativity proposed by Gao et al. (2025) [12], which may influence the spacetime curvature near compact objects and consequently impact the evolution of dense dark matter spikes.

In this context, EMRI systems in which stellar-mass compact objects slowly spiral into SMBH provide high precision probes of the inner gravitational potential. The gravitational waves (GWs) emitted by EMRIs, which are expected to be detected by future space-based observatories such as LISA, encode detailed information about the orbital environment and any distribution of ambient matter [13,14]. During approximately $\sim 10^5$ orbital cycles, even minor perturbations in the gravitational potential, such as those caused by a modified DM spike, can cumulatively produce detectable phase shifts in the gravitational waveform [15–17]. Additionally, recent studies of compact objects such as pulsars indicate that their rotational evolution, including changes in the magnetic inclination and braking index, can influence gravitational wave emission [18]. Although EMRIs involve different systems, these results highlight the sensitivity of gravitational waves to detailed microphysics and dynamics of compact objects, reinforcing the potential of EMRI observations to probe dense dark matter structures around SMBHs.

The structure of this paper is as follows: In Section 2, we introduce the SIDM models; Section 3 presents the classical spike model and the strongly interacting dark matter halo models, including the definition of the dissolution radius and its relation to the black hole mass; Section 4 calculates the gravitational waveforms for circular orbits under the adiabatic approximation; Section 5 analyzes the phase differences induced by different dark matter halo models; finally, Section 6 summarizes the main results and conclusions of this work.

2. Self-Interacting Dark Matter Models

In our work, we consider SIDM as the underlying particle physics framework for constructing dark matter spikes around black holes. SIDM is characterized by strong dark matter self-scattering, which can alleviate small-scale structure problems and naturally generate central halo cores. A common realization is through 2-to-2 elastic scattering, which can be modeled by a scalar dark matter field χ with a quartic self-interaction term, $\mathcal{L} \supset -\lambda_2|\chi|^4$ [2]. Such interactions lead to velocity-dependent cross sections that modify the inner halo profile.

Beyond 2-to-2 scattering, certain SIDM candidates, known as SIMP, undergo $3 \to 2$ or more general $n \to m$ annihilation processes. These interactions can set the plateau density within the spike, $\rho_{\rm pl}^{n\to m}$, and thus determine the dissolution radius $R_{\rm diss}^{n\to m}$ [19,20]. In these models, the dark matter Lagrangian may include cubic and higher-order self-interactions, $\mathcal{L} \supset -\frac{\kappa_3}{3!}\chi^3 - \lambda_4|\chi|^6 + \ldots$, possibly with a discrete Z_3 symmetry, to ensure the stability of dark matter [21]. Such interactions are essential for dynamically generating the plateau region in the spike and for describing arbitrary $n \to m$ annihilation processes.

These SIDM Lagrangians provide the particle physics input for our spike models. In particular, the 2-to-2 and 3-to-2 interactions determine the maximum density (plateau) achievable inside the spike, which in turn sets the size of the dissolution radius $R_{\rm diss}^{n\to m}$. This framework allows us to systematically study the effects of different self-interactions on the dark matter density profile around black holes and on observable signatures such as EMRI gravitational waves or gamma-ray emissions from dark matter annihilation.

In addition to the conventional SIDM framework, both mirror dark matter and nuclear-interacting dark matter may have significant effects on the structure of dark matter spikes around black holes. Mirror dark matter models were first introduced in pioneering work by Blinnikov and Khlopov [22] and later developed in subsequent studies by Berezhiani et al. [23]. These models postulate the existence of mirror particles and interactions that are symmetric with respect to the visible sector, interacting with ordinary matter only via gravity or other ultraweak forces [24]. This symmetry can lead to mirror dark matter forming distributions in gravitational potentials that are similar to ordinary matter, thereby affecting the spike density profile and plateau density. It is worth noting that the SIMP framework, as well as related scenarios such as mirror dark matter (MDM), has been critically examined in the literature. For instance, constraints from neutron-mirror neutron oscillations [25], cosmological simulations [26], and direct detection limits [27] highlight challenges and limitations of mirror dark matter models, including requirements on particle masses, mixing angles, and interaction strengths. These studies provide important context for the assumptions adopted in our spike modeling and underline the need to consider observational bounds when exploring number changing processes in dense dark matter environments.

On the other hand, nuclear-interacting dark matter can form dark atoms through composite interactions with nuclei, with annihilation and dynamical behaviors that differ from those of standard WIMPs or SIDM [28]. Such dark matter may modify the annihilation rate inside the spike and even influence the dissolution radius and plateau density. Considering these properties together allows for a more comprehensive assessment of the microphysical mechanisms shaping black hole spikes, as well as their potential observational signatures in gravitational waves or gamma-ray emissions.

Lagrangians for Self-Interacting Dark Matter

In this work, we consider several possible Lagrangians for SIDM, covering 2-to-2 elastic scattering, 3-to-2 interactions, and more general $n \to m$ annihilation processes, as well as multi-component models with mediator fields.

1. Scalar SIDM with quartic self-interaction (2→2 scattering):

$$\mathcal{L}_\chi = \frac{1}{2}(\partial_\mu \chi)^2 - \frac{1}{2}m_\chi^2 \chi^2 - \frac{\lambda_2}{4}\chi^4. \tag{1}$$

Here, χ is a real scalar dark matter field, and λ_2 controls the 2-to-2 elastic scattering cross section. This type of interaction is commonly used to generate SIDM halo cores [2].

2. SIMP-like scalar with cubic and higher-order interactions (3→2 and $n \to m$ scattering):

$$\mathcal{L}_{\text{SIMP}} = |\partial_\mu \chi|^2 - m_\chi^2 |\chi|^2 - \frac{\kappa_3}{3!}(\chi^3 + \chi^{*3}) - \frac{\lambda_4}{4!}|\chi|^6 + \dots \tag{2}$$

Here, χ is a complex scalar field, with a discrete Z_3 symmetry to ensure stability. The cubic term drives 3→2 scattering, while higher-order terms can generate $n \to m$ interactions [19,20].

3. SIDM with a light mediator (Yukawa-type interactions):

$$\mathcal{L}_{\text{med}} = \frac{1}{2}(\partial_\mu \chi)^2 - \frac{1}{2}m_\chi^2 \chi^2 + \frac{1}{2}(\partial_\mu \phi)^2 - \frac{1}{2}m_\phi^2 \phi^2 - g\chi^2 \phi. \tag{3}$$

The light mediator ϕ allows velocity-dependent cross sections, modifying halo profiles in a scale-dependent way [2].

4. Multi-component SIDM with discrete symmetries:

$$\mathcal{L}_{\text{multi}} = \sum_i \left[|\partial_\mu \chi_i|^2 - m_i^2 |\chi_i|^2 \right] - \sum_{i,j,k} \frac{\kappa_{ijk}}{3!}(\chi_i \chi_j \chi_k + \text{h.c.}) - \sum_{i,j} \lambda_{ij} |\chi_i|^2 |\chi_j|^2 + \dots \tag{4}$$

This framework allows multiple dark matter species with general n→m interactions, controlled by discrete symmetries (e.g., $Z_2 \times Z_3$), to ensure stability [21].

5. General $n \to m$ effective interactions:

$$\mathcal{L}_{n\to m} \supset -\frac{\lambda_{n,m}}{n!}\chi^n - \frac{\lambda_{m,n}}{m!}\chi^{*m} + \text{h.c.} \tag{5}$$

This term is an effective description of general n→m scatterings in the dark sector, which can be matched to microphysical models.

Each of these Lagrangians provides a particle physics input for constructing dark matter spikes around black holes, determining the plateau density $\rho_{\text{pl}}^{n\to m}$ and the corresponding dissolution radius $R_{\text{diss}}^{n\to m}$.

3. Dark Matter Spike Models

In this section, we construct representative dark matter spike models around SMBH, which form the basis for subsequent gravitational wave analyses. We discuss (1) the classical collisionless spike, (2) spikes modified by dark matter annihilation ($2 \to 0$ process), and (3) spikes affected by self-interactions and number changing processes such as $2 \to 2$ and $3 \to 2$ reactions.

3.1. Classical Spike Model

The classical spike forms due to the adiabatic growth of an SMBH inside a collisionless CDM halo. Assuming an initial power-law density profile $\rho_\chi(r) \propto r^{-\gamma}$, the spike develops a steeper power law near the black hole [5]:

$$\rho_{\text{sp}}(r) = \rho_R \left(\frac{R}{r}\right)^{\gamma_{\text{sp}}}, \quad \gamma_{\text{sp}} = \frac{9 - 2\gamma}{4 - \gamma}, \tag{6}$$

where R is the spike radius, ρ_R is the density at R, and r ranges between the Schwarzschild radius and R. For typical NFW halos with $\gamma = 1$, this gives $\gamma_{\text{sp}} = 7/3$.

3.2. Spike Model with Dark Matter Annihilation 2 to 0

Dark matter annihilation in the spike core can flatten the density, forming a saturated region where annihilation balances the inflow. The saturated density is given by [29]:

$$\rho_{\rm sat} = \frac{m_\chi}{\langle\sigma v\rangle t_{\rm BH}}, \tag{7}$$

where m_χ is the DM mass, $\langle\sigma v\rangle$ is the annihilation cross section, and $t_{\rm BH}$ is the SMBH age. The spike density becomes:

$$\rho_\chi(r) = \begin{cases} \rho_{\rm sat}, & r < r_{\rm sat} \\ \rho_{\rm sp}(r), & r \geq r_{\rm sat} \end{cases}, \tag{8}$$

with $r_{\rm sat}$ being the radius where $\rho_{\rm sp}(r_{\rm sat}) = \rho_{\rm sat}$.

3.3. Spike Models with 2-to-2 and 3-to-2 Processes

Self-interactions between dark matter particles, including elastic scattering ($2 \to 2$) and number changing processes such as semi-annihilation ($3 \to 2$), play a central role in the SIMP framework. In this scenario, dark matter particles maintain chemical equilibrium in the early universe through these number changing reactions, which primarily determine the relic density rather than annihilations with Standard Model particles [3,30]. Such interactions not only reduce the total dark matter abundance but also inject kinetic energy into the dark matter halo, for example in spikes around SMBH, thereby heating the spike and potentially flattening or softening its density profile. The relaxation time scale for elastic scattering is as follows:

$$t_{\rm relax}(r) \sim \frac{1}{n_\chi \sigma_{\rm self} v}, \tag{9}$$

where n_χ is the DM number density, $\sigma_{\rm self}$ is the self-interaction cross section, and v is the typical velocity.

Number changing reactions such as $3 \to 2$ reduce DM number density and inject kinetic energy, which can be modeled by an evolution equation:

$$\frac{d\rho_\chi}{dt} \propto -\langle\sigma v^2\rangle_{3\to2}\rho_\chi^3. \tag{10}$$

These processes can flatten or even dissolve the spike core depending on reaction rates and interaction strengths [31]. For instance, the annihilation rate required to significantly flatten the DM spike is $\langle\sigma v\rangle \sim 10^{-24}$ cm^3/s, while observational constraints from Fermi-LAT set an upper limit of $\langle\sigma v\rangle \lesssim 2 \times 10^{-25}$ cm^3/s for similar DM masses [32]. This indicates that only a fraction of the considered parameter space is allowed in realistic astrophysical scenarios.

We adopt analytical spike profiles reflecting these effects and use them in the later gravitational waveform calculations.

3.4. Dark Matter Dissolution Effects from Number Changing Processes

In general, the interaction rate of an $N \to M$ dark matter process can be understood by considering the probability for one particle to find $(n-1)$ partners to interact with. The total reaction rate per unit volume and per unit time scales is as follows:

$$R_{n\to m} \sim n_\chi^n \langle\sigma v^{n-1}\rangle, \tag{11}$$

where n_χ is the number density of dark matter, and $\langle \sigma v^{n-1} \rangle$ denotes the generalized thermally averaged cross section with appropriate velocity factors to ensure the correct dimensionality.

For a single particle, the effective scattering rate is obtained by dividing by n_χ:

$$\Gamma_\chi \sim n_\chi^{n-1} \langle \sigma v^{n-1} \rangle. \tag{12}$$

This expression shows that higher-order processes become increasingly suppressed at a low number density, since each additional incoming particle contributes an extra factor of n_χ.

As concrete examples, for $2 \to 2$ processes, one finds $\Gamma_\chi \sim n_\chi \langle \sigma v \rangle$; for $3 \to 2$ processes, $\Gamma_\chi \sim n_\chi^2 \langle \sigma v^2 \rangle$, and so forth. Thus, the scaling with n_χ^{n-1} is a direct consequence of the need for $(n-1)$ additional particles to participate in the interaction.

We now analyze how number changing interactions of DM, such as the $2 \to 0$ annihilation and the general $n \to m$ transitions, can lead to the depletion or modification of DM density spikes. The temporal evolution of the DM number density at a fixed radius r, denoted as $n_\chi(r,t)$, follows the equation below:

$$\dot{n}_\chi(r,t) = -\langle \sigma_{2\to 0} v \rangle n_\chi^2(r,t) - \frac{1}{n!} \langle \sigma_{n\to m} v^{n-1} \rangle n_\chi^n(r,t), \tag{13}$$

assuming identical particles in the initial state. The factors $1/2$ and $1/n!$ account for the symmetry of the initial states in the $2 \to 0$ and $n \to m$ processes, respectively. In these reactions, either 2 or n DM particles are depleted, and the products in the final state are relativistic. Hence, the outgoing particles escape the gravitational potential at radius r, effectively erasing all contributing particles from the density profile.

As the initial condition for solving this equation, we set $n_\chi(r, t_{\rm ini}) = \rho_\chi(r, t_{\rm ini})/m_\chi$, where $\rho_\chi(r, t_{\rm ini})$ is the density profile formed prior to significant annihilation. This assumption is valid because spike formation generally occurs on shorter timescales than the typical age of the DM distribution.

To proceed analytically, suppose a single dominant number changing process, labeled $N \to M$, governs the evolution. Integrating the above equation from the spike formation epoch $t_{\rm ini}$ to the present time $t = t_{\rm age}$, our results are consistent with those reported in [33]:

$$\rho_\chi(r,t) = \frac{\rho_{{\rm pl},N\to M}\, \rho_\chi(r, t_{\rm ini})}{\left[\rho_{{\rm pl},N\to M}^{N-1} + \rho_\chi^{N-1}(r, t_{\rm ini})\right]^{1/(N-1)}}, \tag{14}$$

with the plateau density defined as follows:

$$\rho_{{\rm pl},N\to M} \equiv m_\chi \left[\frac{(N-2)!}{\langle \sigma_{N\to M} v^{N-1} \rangle t_{\rm age}}\right]^{1/(N-1)}. \tag{15}$$

This plateau value represents the maximum sustainable density under the given process. Explicitly, for representative cases relevant to strong self-interaction and $n \to m$ transitions, we have the following:

$$\rho_{{\rm pl},2\to 0} = \frac{m_\chi}{\langle \sigma_{2\to 0} v \rangle t_{\rm age}}, \tag{16}$$

$$\rho_{{\rm pl},3\to 2} = m_\chi \left(\frac{1}{\langle \sigma_{3\to 2} v^2 \rangle t_{\rm age}}\right)^{1/2}, \tag{17}$$

$$\rho_{{\rm pl},4\to 2} = m_\chi \left(\frac{1}{\langle \sigma_{4\to 2} v^3 \rangle t_{\rm age}}\right)^{1/3}. \tag{18}$$

In scenarios where multiple number changing processes are relevant, Equation (13) must be solved numerically. Similar to the transition radii that define the boundaries of isothermal or self-heated cores, we introduce the "dissolution radius" $R_{\rm diss}$, which separates regions where the initial profile remains intact from those capped by the plateau density.

To demonstrate the combined influence of gravitational and particle physics effects on spike structure, we adopt an initial NFW profile, with a central SMBH of mass $M_{\rm BH} \approx 4.15 \times 10^6 M_\odot$, forming a DM spike of scale $R_{\rm sp} \sim 18.7\,{\rm pc}$ and slope $\gamma_{\rm sp} = 7/3$. While in the Milky Way this spike may be reduced by stellar heating, other galaxies without such dynamical disruptions can retain prominent spikes. We use this fiducial model to assess how SIDM and $n \to m$ transitions affect the gravitational wave signatures from EMRIs traversing these environments.

In Table 1, we summarize several representative dark matter number changing and conserving processes, following [33]. The conventional $2 \to 0$ annihilation channel transfers all of the DM rest mass energy into Standard Model states, while the $2 \to 1$ semi-annihilation process leaves one DM particle in the final state together with a light SM particle. Elastic $2 \to 2$ scatterings conserve the DM number but redistribute kinetic energy, leading to the formation of isothermal cores through multiple scatterings. In contrast, higher-order processes such as $3 \to 2$ and $4 \to 2$ play a central role in SIMP models, where strong self-interactions are invoked to determine the relic abundance at sub-GeV scales. For completeness, typical cross section values for $4 \to 2$ processes are $\langle \sigma v^3 \rangle \sim 10^{-32}\,{\rm cm}^6/{\rm s}$, based on SIMP models (Hochberg et al., 2014) [3]. The characteristic final-state DM kinetic energies shown in the last column highlight the potential importance of self-heating effects, which can reshape the central density profile of dark matter spikes around supermassive black holes.

Table 1. Comparison of representative $n \to m$ dark matter processes. The table summarizes the key reaction channels, their theoretical frameworks, the typical dark matter mass scales suggested by cosmological considerations, and the characteristic kinetic energy E_χ carried by the final-state DM particles.

Process	Reaction	Typical Framework	DM Mass Scale	E_χ of Final State DM
$2 \to 0$	$\chi\chi \to$ SM particles	Standard annihilation	Model dependent	None (all energy to SM)
$2 \to 1$	$\chi\chi \to \chi + {\rm SM}$	Semi-annihilation (requires light SM particle, e.g., ν, γ)	Model dependent	$\simeq \frac{5}{4} m_\chi$
$2 \to 2$	$\chi\chi \to \chi\chi$	Elastic self-scattering	Model dependent	$\simeq m_\chi$ (energy redistributed)
$3 \to 2$	$\chi\chi\chi \to \chi\chi$	SIMP (Strongly Interacting Massive Particle)	$\mathcal{O}(100)\,{\rm MeV}$	$\simeq \frac{3}{2} m_\chi$
$4 \to 2$	$\chi\chi\chi\chi \to \chi\chi$	SIMP framework (self-conjugate DM: real scalar, Majorana fermion, sterile neutrino)	$\mathcal{O}(100)\,{\rm keV}$	$\simeq 2 m_\chi$

3.5. Characteristic Radii: Dissolution and Cutoff

In addition to the isothermal and self-heating cores, the DM spike is affected by number changing processes. We define the dissolution radius $R_{\rm diss}$ as the radius inside which the DM density is significantly reduced due to $n \to m$ processes.

For a dominant $N \to M$ process, the condition for efficient depletion within the halo age $t_{\rm age}$ reads as follows:

$$n_\chi(R_{\rm diss})^{N-1} \langle \sigma_{N\to M} v^{N-1} \rangle \, t_{\rm age} \simeq 1\,, \tag{19}$$

where $n_\chi(R_{\rm diss})$ is the DM number density at $R_{\rm diss}$. Solving for the density, we obtain the following:

$$n_\chi(R_{\rm diss}) \;=\; \left[\frac{1}{\langle\sigma_{N\to M} v^{N-1}\rangle\, t_{\rm age}}\right]^{\frac{1}{N-1}}. \tag{20}$$

This density corresponds to the plateau density $\rho_{\rm pl} = m_\chi n_\chi(R_{\rm diss})$; for $r < R_{\rm diss}$, the DM profile is flattened, while for $r > R_{\rm diss}$, the initial spike profile remains approximately unmodified.

Furthermore, the spike profile can be truncated at a minimum radius $r_{\rm cut}$ due to either self-annihilation or other maximal density limits. An approximate expression for $r_{\rm cut}$ is as follows:

$$r_{\rm cut} \sim 10^{-7}\, h^{-1}\ {\rm kpc}\left(\frac{m_{\rm DM}}{100\ {\rm GeV}}\right)^{1/\gamma}\left(\frac{3\times 10^{-26}\ {\rm cm}^3/{\rm s}}{\langle\sigma v\rangle}\right)^{1/\gamma}\left(\frac{1\ M_\odot}{M_{\rm BH}}\right)^{1/3}, \tag{21}$$

where γ is the inner slope of the initial DM profile and $M_{\rm BH}$ is the mass of the central supermassive black hole.

In numerical calculations and plotting, the radius $R_{\rm diss}$ can be found by solving $n_\chi(R_{\rm diss}) = \rho_{\rm pl}/m_\chi$, and the profile is truncated at $r_{\rm cut}$ if necessary.

3.6. Dissolution Radius $R_{\rm diss}$ for General $n \to m$ DM Number Changing Processes

We consider a single dominant $N \to M$ DM number changing process, for which the evolution of the DM number density is given by the following:

$$\frac{dn_\chi(r,t)}{dt} = -\langle\sigma_{N\to M} v^{N-1}\rangle\, n_\chi(r,t)^N, \tag{22}$$

with the initial number density $n_\chi(r, t_{\rm ini}) = n_\chi^{\rm ini}(r)$. To estimate the radius where the DM spike is significantly dissolved over the halo age $t_{\rm age}$, we define the dissolution radius $R_{\rm diss}$ by:

$$n_\chi(R_{\rm diss})^{N-1}\,\langle\sigma_{N\to M} v^{N-1}\rangle\, t_{\rm age} \simeq 1\,. \tag{23}$$

Inside the spike, the DM density is often approximated as a power law:

$$\rho_\chi(r) = \rho_{\rm spike}(r) = \rho_R\left(\frac{r}{R_{\rm spike}}\right)^{-\gamma_{\rm sp}}, \tag{24}$$

so that the number density is $n_\chi = \rho_\chi/m_\chi$. Substituting this into the previous equation gives the following:

$$\frac{\rho_R}{m_\chi}\left(\frac{R_{\rm diss}}{R_{\rm spike}}\right)^{-\gamma_{\rm sp}} = \left[\frac{1}{\langle\sigma_{N\to M} v^{N-1}\rangle\, t_{\rm age}}\right]^{\frac{1}{N-1}}. \tag{25}$$

Taking the $-1/\gamma_{\rm sp}$ power of both sides, we obtain a general expression for the dissolution radius:

$$R_{\rm diss} = R_{\rm spike}\left[\frac{\rho_R}{m_\chi}\left(\langle\sigma_{N\to M} v^{N-1}\rangle\, t_{\rm age}\right)^{\frac{1}{N-1}}\right]^{\frac{1}{\gamma_{\rm sp}}}, \tag{26}$$

where $N = 2, 3, 4, \ldots$ corresponds to different $n \to m$ processes; $\gamma_{\rm sp}$ is the power-law index of the spike; ρ_R is the normalization density of the spike; and $t_{\rm age}$ is the age of the halo or the region around the SMBH.

Special Cases

For the $2 \to 0$ annihilation process,

$$R_{\text{diss}}^{2\to 0} = R_{\text{spike}} \left(\frac{\rho_R}{m_\chi} \langle \sigma_{2\to 0} v \rangle t_{\text{age}} \right)^{1/\gamma_{\text{sp}}}. \tag{27}$$

For the $3 \to 2$ process,

$$R_{\text{diss}}^{3\to 2} = R_{\text{spike}} \left[\frac{\rho_R}{m_\chi} \left(\langle \sigma v^2 \rangle \, t_{\text{age}} \right)^{1/2} \right]^{1/\gamma_{\text{sp}}}. \tag{28}$$

This expression is consistent in spirit with the r_{cut} formula often used for the $2 \to 0$ annihilation process with explicit numerical estimates.

Figure 1 demonstrates how the inner depletion of a dark matter spike is influenced by number changing processes. The dissolution radius R_{diss} grows both with an increasing interaction cross section and with the assumed age of the dark matter halo. While the figure explicitly shows only the $2 \to 0$ annihilation (left panel) and the $3 \to 2$ self-interaction (right panel), other processes such as $2 \to 1$ semi-annihilation and $4 \to 2$ interactions follow similar trends. The $2 \to 1$ process behaves qualitatively like $2 \to 0$, whereas $4 \to 2$ behaves like $3 \to 2$ but requires larger cross sections. This demonstrates that the scale of depletion in the spike is set jointly by particle physics parameters and astrophysical conditions.

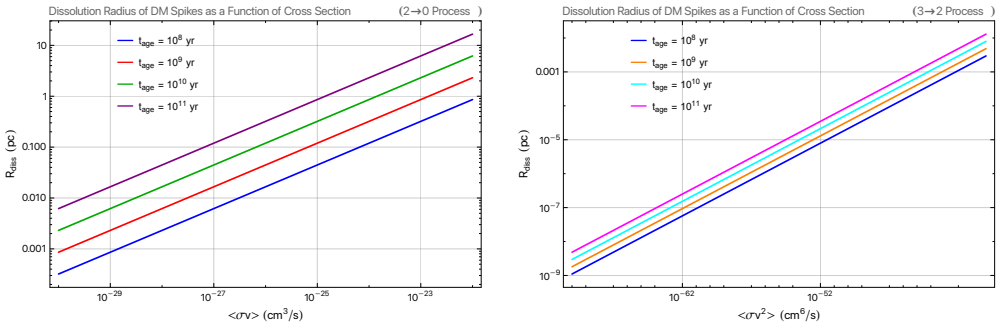

Figure 1. Dissolution radius R_{diss} as a function of the dark matter cross section for two representative number changing processes. **Left:** $2 \to 0$ annihilation process. **Right:** $3 \to 2$ self-interaction process. Different curves correspond to different assumed dark matter halo ages, illustrating how R_{diss} increases with both the cross section and the halo age.

3.7. Relation Between Dissolution Radius and Black Hole Mass

The influence radius of a black hole is defined as follows:

$$r_h = \frac{G M_{\text{BH}}}{\sigma_*^2}, \tag{29}$$

where M_{BH} is the black hole mass and σ_* is the velocity dispersion of the host galaxy.

Typically, the spike radius is taken as a fraction of the influence radius:

$$R_{\text{spike}} \sim \alpha \, r_h = \alpha \frac{G M_{\text{BH}}}{\sigma_*^2}, \qquad (\alpha \sim 0.1\text{–}0.2). \tag{30}$$

In the classical Gondolo–Silk model, the spike density profile is written as follows:

$$\rho(r) = \rho_R \left(\frac{R_{\text{spike}}}{r} \right)^{\gamma_{\text{sp}}}, \tag{31}$$

where γ_{sp} is typically ~ 2.25. At $r = R_{spike}$,

$$\rho_R \sim \rho(r_h) \sim \rho_0 \left(\frac{r_0}{r_h}\right)^{\gamma_c}, \tag{32}$$

with γ_c being the inner slope of the original dark matter halo (e.g., $\gamma_c = 1$ for an NFW profile). Hence,

$$\rho_R \propto r_h^{-\gamma_c} \propto M_{BH}^{-\gamma_c}. \tag{33}$$

Furthermore, the dissolution radius can be expressed as follows:
For $2 \to 0$ annihilation,

$$R_{diss}^{2\to 0} \sim \left(\frac{\rho_R}{m_\chi}\langle\sigma v\rangle t_{age}\right)^{1/\gamma_{sp}} \frac{GM_{BH}}{\sigma_*^2}. \tag{34}$$

For $3 \to 2$ process,

$$R_{diss}^{3\to 2} \sim \frac{\rho_R}{m_\chi}^{1/\gamma_{sp}} \left(\langle\sigma v^2\rangle t_{age}\right)^{1/2\gamma_{sp}} \frac{GM_{BH}}{\sigma_*^2}. \tag{35}$$

Thus, the dependence of the dissolution radius on the black hole mass is as follows:

$$R_{diss}^{2\to 0} \propto M_{BH}^{1-\gamma_c/\gamma_{sp}}, \tag{36}$$

$$R_{diss}^{3\to 2} \propto M_{BH}^{1-\gamma_c/\gamma_{sp}}. \tag{37}$$

For example, with $\gamma_c = 1$ and $\gamma_{sp} = 7/3$, the exponents are as follows:

$$R_{diss}^{2\to 0} \propto M_{BH}^{0.57}, \qquad R_{diss}^{3\to 2} \propto M_{BH}^{0.57}. \tag{38}$$

This indicates that black holes with larger masses correspond to larger dissolution radii.

Figure 2 shows how the dissolution radius R_{diss} depends on the black hole mass M_{BH} for two different dark matter annihilation processes. As M_{BH} increases, R_{diss} also increases, indicating that more massive black holes correspond to larger regions where the dark matter spike is significantly depleted.

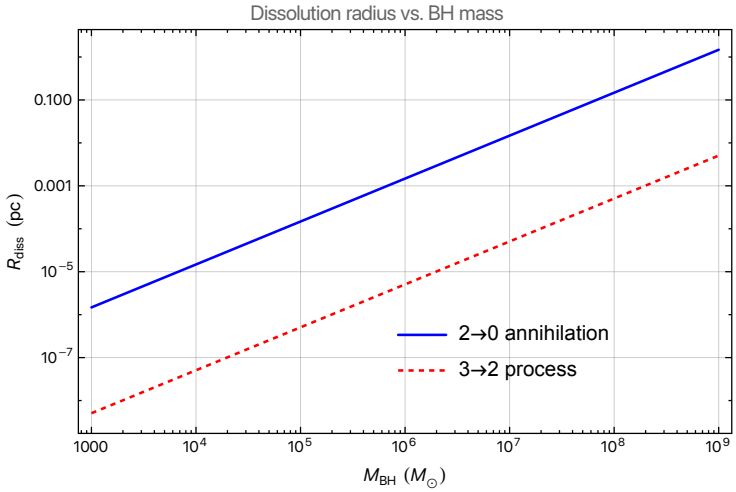

Figure 2. Dissolution radius R_{diss} as a function of black hole mass M_{BH} for different dark matter annihilation processes. The solid blue line represents the $2 \to 0$ annihilation, and the dashed red line represents the $3 \to 2$ process. Calculations assume $\rho_R = 240.3$ GeV/cm^3, $m_\chi = 0.01$ GeV, $\sigma_* = 100$ km/s, $\alpha = 0.2$, and spike slope $\gamma_{sp} = 7/3$.

Comparing the two processes, the $3 \to 2$ annihilation and the $2 \to 0$ annihilation show similar growth trends with $M_{\rm BH}$. This is consistent with the theoretical scaling relations, namely $R_{\rm diss}^{2\to0} \propto M_{\rm BH}^{1-\gamma_c/\gamma_{\rm sp}}$ and $R_{\rm diss}^{3\to2} \propto M_{\rm BH}^{1-\gamma_c/\gamma_{\rm sp}}$, which indicate that both annihilation mechanisms have the same mass dependence on the black hole.

For low-mass black holes (10^3–10^5 $M_\odot$), the dissolution radius is relatively small, suggesting that the spike remains mostly intact. For SMBH (10^8–10^9 $M_\odot$), $R_{\rm diss}$ can reach approximately 0.01 pc, implying significant depletion of the inner spike, which could impact gravitational wave signals from EMRIs systems.

Overall, the figure demonstrates that both the black hole mass and the type of dark matter self-interaction play a crucial role in determining the size of the dissolution region around black holes.

The dark matter density around a black hole, taking into account the innermost stable circular orbit (ISCO) and possible $n \to m$ annihilation processes, can be modeled as a piecewise function:

$$\rho(r) = \begin{cases} 0, & r \le R_{\rm ISCO}, \\ \rho_{\rm pl}^{n\to m}, & R_{\rm ISCO} < r \le R_{\rm diss}^{n\to m}, \\ \rho_R \left(\dfrac{R_{\rm spike}}{r}\right)^{\gamma_{\rm sp}}, & R_{\rm diss}^{n\to m} < r \le R_{\rm spike}, \\ \rho_{\rm halo}(r), & r > R_{\rm spike}. \end{cases} \tag{39}$$

Here, $R_{\rm ISCO}$ denotes the innermost stable circular orbit inside which dark matter cannot survive due to the strong gravitational field of the black hole, so the density is effectively zero. The plateau density, $\rho_{\rm pl}^{n\to m}$, is set by the $N \to M$ annihilation process and represents the maximum density that dark matter can reach within the spike. $R_{\rm diss}^{n\to m}$ is the dissolution radius where the spike density decreases to the plateau value. The spike radius $R_{\rm spike}$ is determined by the black hole's gravitational influence, usually taken as a fraction of the black hole's sphere of influence, and $\gamma_{\rm sp}$ characterizes the steep power-law index of the spike. The density at the spike edge, $\rho_R = \rho(R_{\rm spike}) \sim \rho_0 (r_0/r_h)^{\gamma_c}$, is set by the original halo profile, while $\rho_{\rm halo}(r)$ represents the unperturbed halo density outside the spike, for example, an NFW profile [34]:

$$\rho_{\rm halo}(r) = \frac{\rho_0}{(r/r_s)(1+r/r_s)^2}. \tag{40}$$

This four-region model intuitively captures the main features of dark matter distribution near a black hole. Within the ISCO, the density vanishes due to strong gravitational forces. Between $R_{\rm ISCO}$ and $R_{\rm diss}^{n\to m}$, the density is flattened to the plateau value due to $n \to m$ annihilation. From $R_{\rm diss}^{n\to m}$ to $R_{\rm spike}$, the density rises steeply following the spike power law, and beyond $R_{\rm spike}$, the density returns to the original halo profile. This model provides a physically motivated framework suitable for studies of EMRI gravitational waves or gamma-ray signals from dark matter spikes.

Figure 3 shows the radial dark matter spike profiles for different annihilation and scattering processes. It can be seen that higher-order processes such as 3→2 exhibit a higher plateau density, $\rho_{\rm pl}^{3\to2}$, but a smaller dissolution radius, $R_{\rm diss}^{3\to2}$. This is because 3→2 scatterings are more efficient, depleting the central dark matter more rapidly over the system age $t_{\rm age}$, resulting in a more concentrated density profile. For each process, the plateau density $\rho_{\rm pl}^{N\to M}$ and the dissolution radius $R_{\rm diss}^{N\to M}$ are computed using the respective annihilation or scattering cross section $\langle \sigma_{N\to M} v^{N-1} \rangle$, dark matter mass m_χ, and the system age, combined with a spike power-law index $\gamma_{\rm sp}$ to construct a four-segment piecewise model. Physically, these models apply to dark matter halos surrounding supermassive black

holes, with different $n \to m$ processes reflecting distinct microscopic interactions: 2→0 for standard WIMP annihilation, 2→2 for elastic SIDM scattering, and 3→2 for SIMP-like strongly interacting dark matter. The figure illustrates how higher-order interactions lead to denser central plateaus and smaller dissolution radii, which has important implications for SMBH environments, gravitational wave signals, and indirect dark matter detection.

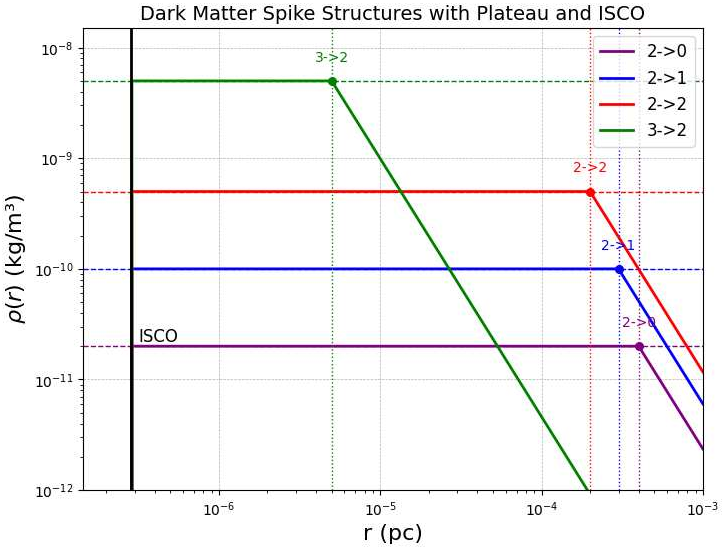

Figure 3. Dark matter spike density profiles around a supermassive black hole of mass $10^6\, M_\odot$. Horizontal dashed lines indicate plateau densities, and colored dotted vertical lines mark the dissolution radii. The black solid vertical line represents the innermost stable circular orbit (ISCO) at $r_{\rm ISCO} = 2.87 \times 10^{-7}$ pc. Colored dots indicate the corresponding plateau densities at the dissolution radii for transitions $2 \to 0$, $2 \to 1$, $2 \to 2$, and $3 \to 2$.

4. Waveform Modeling and Orbital Dynamics

In this study, we neglect the effects of gas and stellar perturbations on EMRI evolution. This is justified because, for typical EMRIs in galactic nuclei, the gravitational influence of the central supermassive black hole and the dark matter spike dominates over gas drag and stellar encounters, which induce only minor corrections to the orbital dynamics [35–40].

4.1. Equation of Motion for the Stellar-Mass Compact Object

We consider an EMRI system composed of a stellar-mass black hole of mass μ orbiting a supermassive black hole of mass $M_{\rm BH}$, with $\mu \ll M_{\rm BH}$. We adopt a reference frame centered at the system barycenter, which approximately coincides with the position of the supermassive black hole. The radial separation r between the two black holes evolves according to the following:

$$\frac{d^2r}{dt^2} = -\frac{GM_{\rm eff}}{r^2} - \frac{F}{r^{\alpha-1}} + \frac{h^2}{r^3}, \tag{41}$$

where h is the specific angular momentum of the stellar-mass object, $M_{\rm eff}$ is the effective central mass including DM depletion within the ISCO, and F parametrizes the gravitational influence of the DM spike beyond the ISCO radius [41]. Explicitly,

$$M_{\rm eff} = \begin{cases} M_{\rm BH} - M_{\rm DM}(< r_{\rm min}), & r_{\rm min} \le r \le r_{\rm sp}, \\ M_{\rm BH}, & r < r_{\rm min}, \end{cases} \tag{42}$$

$$F = \begin{cases} r_{\min}^{\alpha-3} M_{\mathrm{DM}}(< r_{\min}), & r_{\min} \le r \le r_{\mathrm{sp}}, \\ 0, & r < r_{\min}, \end{cases} \tag{43}$$

where $M_{\mathrm{DM}}(< r_{\min})$ is the DM mass enclosed within $r_{\min}$, and α is the power-law index of the DM spike.

The terms on the right hand side represent, respectively, the gravitational pull from the effective central mass, the DM spike's additional gravitational force, and the centrifugal force. Dissipative effects such as dynamical friction and GW backreaction are initially neglected in Equation (41).

4.2. Orbital Frequency and Circular Orbit Condition

Assuming a quasicircular orbit ($d^2r/dt^2 = 0$), the orbital radius R satisfies

$$\omega_s^2 = \frac{GM_{\mathrm{eff}}}{R^3} + \frac{F}{R^\alpha}, \tag{44}$$

where ω_s is the orbital angular frequency. In the absence of DM spikes ($F \to 0$ and $M_{\mathrm{eff}} \to M_{\mathrm{BH}}$), Equation (44) reduces to the standard Keplerian expression.

4.3. Energy Balance and Orbital Evolution

Including GW emission and dynamical friction effects, the orbital energy E_{orbit} evolves according to the energy balance equation:

$$-\frac{dE_{\mathrm{orbit}}}{dt} = \frac{dE_{\mathrm{GW}}}{dt} + \frac{dE_{\mathrm{DF}}}{dt}. \tag{45}$$

The orbital energy for a circular orbit is as follows:

$$E_{\mathrm{orbit}} = -\frac{G\mu M_{\mathrm{eff}}}{2R} + \frac{4-\alpha}{2(2-\alpha)}\mu\frac{F}{R^{\alpha-2}}. \tag{46}$$

The GW energy loss rate at leading (quadrupole) order is as follows [42]:

$$\frac{dE_{\mathrm{GW}}}{dt} = \frac{32}{5}\frac{G\mu^2}{c^5}R^4\omega_s^6. \tag{47}$$

The dynamical friction loss due to interaction with DM particles is approximated by the following [43]:

$$\frac{dE_{\mathrm{DF}}}{dt} = 4\pi G^2\mu^2\rho_{\mathrm{DM}}(r)\ln\Lambda\frac{1}{v}, \tag{48}$$

where $\rho_{\mathrm{DM}}(r)$ is the local DM density, $v \approx R\omega_s$ is the orbital velocity, and $\ln\Lambda$ is the Coulomb logarithm.

From the energy balance Equation (45), one obtains the orbital radius evolution dR/dt, which determines the inspiral rate and thus the gravitational waveform phase evolution.

4.4. Gravitational Waveform

The leading-order GW polarizations emitted by the binary are given by the following:

$$h_+(t) = \frac{4G\mu\omega_s^2R^2}{c^4D}\frac{1+\cos^2\iota}{2}\cos\Phi(t), \tag{49}$$

$$h_\times(t) = \frac{4G\mu\omega_s^2R^2}{c^4D}\cos\iota\sin\Phi(t), \tag{50}$$

where D is the source distance, ι is the inclination angle, and $\Phi(t) = \int\omega_{\mathrm{GW}}(t)dt$ is the GW phase with $\omega_{\mathrm{GW}} = 2\omega_s$. The slowly shrinking orbit due to the radiation reaction

and friction causes a time-dependent amplitude and frequency, making the waveform quasicircular and adiabatically evolving.

The Fourier transform of the waveform can be computed using the stationary phase approximation, yielding an expression that encodes the DM spike effects via $M_{\rm eff}$, F, and α, enabling parameter inference from observed waveforms.

In the presence of a dark matter spike, the frequency-domain GW waveform for an EMRI can be expressed as follows [41]:

$$\tilde{h}(f) = A f^{-7/6} e^{i\Psi(f)}, \tag{51}$$

$$\tilde{\Phi}(f) = \frac{10}{3}\left(\frac{8\pi G M}{c^3}\right)^{-5/3}\left[-f\int_f^{f_{\rm ISCO}} f_0^{-11/3} L^{-1}(f_0) df_0 + \int_f^{f_{\rm ISCO}} f_0^{-8/3} L^{-1}(f_0) df_0\right], \tag{52}$$

$$L(f) = 1 + 4\,c\,\epsilon\,\delta^{\frac{11-2\alpha}{2(3-\alpha)}}, \tag{53}$$

$$\delta = \left(\frac{\pi^2}{G} f^2\right)^{\frac{3-\alpha}{3}}, \tag{54}$$

$$c\epsilon = \frac{5\pi c^5}{G^{5/2}} M_{\rm eff}^{\frac{\alpha+5}{3}} \rho_{\rm sp} r_{\rm sp}^{\alpha} \ln\Lambda, \tag{55}$$

where $M_{\rm eff}$ is the effective central mass, α is the spike power-law index, $\rho_{\rm sp}$ and $r_{\rm sp}$ are the characteristic spike density and radius, and $f_{\rm ISCO}$ is the GW frequency at the innermost stable circular orbit. These formulas show that the DM spike modifies the GW phase $\tilde{\Phi}(f)$ through $L(f)$, producing potentially observable effects.

5. Gravitational Wave Signal and Phase Shift

The GW signal emitted by an EMRI system encodes detailed information about the orbital dynamics of the inspiraling compact object. A key observable is the GW phase $\phi(t)$, which accumulates over the inspiral and is highly sensitive to perturbations in the orbital evolution caused by the surrounding environment, such as a dark matter spike.

The total accumulated phase can be expressed as follows:

$$\phi(t) = \int \omega(t)\, dt, \tag{56}$$

where $\omega(t)$ is the instantaneous orbital angular frequency. The presence of dynamical friction due to an SIDM spike modifies the inspiral rate and hence the phase evolution. To quantify this effect, we define the phase shift relative to the vacuum inspiral as follows:

$$\Delta\phi = \phi_{\rm SIDM} - \phi_{\rm vac}, \tag{57}$$

where $\phi_{\rm SIDM}$ and $\phi_{\rm vac}$ denote the GW phases with and without the SIDM spike, respectively.

Using the orbital evolution equations incorporating both gravitational radiation reaction and dynamical friction, we numerically integrate to obtain $\phi(t)$ and compute $\Delta\phi$. Our calculations indicate that the phase shift accumulates significantly over the last years to months of inspiral, entering the sensitivity band of detectors like *LISA*.

In realistic observations, one cannot obtain a reference signal for the same black hole in a vacuum. Therefore, the phase shift induced by a DM spike may be partially degenerate with other alternatives, such as different DM halo profiles. Nevertheless, our analysis provides theoretical templates to explore the potential influence of DM spikes on EMRI gravitational waves, which may guide future observational studies and help distinguish between different DM models.

In Figure 4, the cumulative phase difference $\Delta\phi$ is largest for the $3\to2$ process, because its plateau density $\rho_{\rm pl}^{3\to2}$ is the highest among the considered channels, leading to the

strongest gravitational effect from dark matter. The typical phase resolution of space-based gravitational wave detectors is about 0.1 Rad [44,45], while the phase differences $\Delta\phi_{n\to m}$ for all channels exceed this threshold, indicating that the detectors can distinguish whether dark matter annihilation occurs within the spike. For a typical EMRI system, the phase measurement uncertainty scales inversely with the signal-to-noise ratio (SNR), $\delta\phi \sim 1/\mathrm{SNR}$ [44]. For a representative EMRI with SNR ~ 30, this gives $\delta\phi \sim 0.03$ rad, which is smaller than the predicted phase shift induced by the DM spike, $\Delta\phi \sim 0.1$ rad, indicating that the effect is potentially detectable by a space-based detector such as *LISA*. Moreover, the relative phase differences $\Delta\phi_{n\to m} - \Delta\phi_{n'\to m'}$ between the four curves are also clearly larger than 0.1 rad, showing that gravitational wave observations can differentiate the four scattering channels. Combined with the relation between the dissolution radius $R_{\mathrm{diss}}^{n\to m}$ and the plateau density $\rho_{\mathrm{pl}}^{n\to m}$, this provides a potential observational probe to test and discriminate different SIDM spike models.

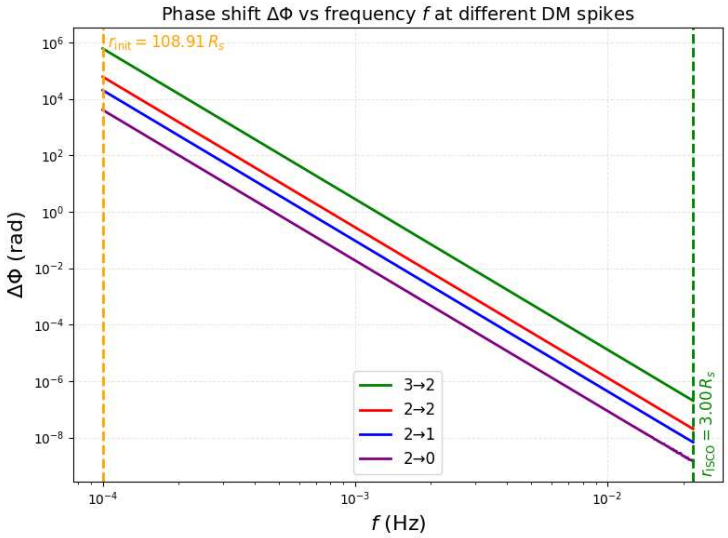

Figure 4. Dark matter spike density profiles around a supermassive black hole of mass $10^5\,M_\odot$. Phase shift $\Delta\Phi$ of gravitational waves from an EMRI as a function of gravitational wave frequency f for different dark matter spike scenarios. The colored curves correspond to different spike models labeled as 3→2, 2→2, 2→1, and 2→0. The vertical green dashed line indicates the innermost stable circular orbit (ISCO) at r_{ISCO} in units of the Schwarzschild radius R_s, while the orange dashed line marks the initial EMRI separation r_{init} corresponding to $f_{\mathrm{GW}} = 10^{-4}$ Hz.

Comparing different $n \to m$ scattering processes, we find that spikes formed by the $3 \to 2$ process exhibit higher plateau densities than those formed by $2 \to 2$ or $2 \to 1$ processes, leading to stronger gravitational effects from dark matter and characteristic differences in the cumulative phase shift $\Delta\phi$. These differences can be distinguished with sufficiently precise waveform measurements.

6. Summary and Discussion

In this work, we have explored the potential of EMRIs to probe SIDM through the formation of spikes induced by number changing processes such as $2 \to 0$, $2 \to 1$, $2 \to 2$, and $3 \to 2$ scatterings. We constructed representative SIDM spike models, incorporating plateau densities, spike regions, and smooth transitions to the outer halo. A key development in this study is the general definition of the dissolution radius $R_{\mathrm{diss}}^{n\to m}$, which quantifies the inner region where number changing interactions significantly alter the dark matter density. For illustrative purposes, explicit calculations for the $2 \to 0$ and $3 \to 2$ processes were provided, and the dependence of $R_{\mathrm{diss}}^{n\to m}$ on the central black hole mass M_{BH} was analyzed.

Using these spike models, we calculated the orbital evolution of EMRIs systems under circular orbit approximation, incorporating the effects of dynamical friction. The resulting gravitational wave phase shifts $\Delta\phi_{n\to m}$ exhibit characteristic differences for each $N \to M$ process. In particular, the $3 \to 2$ process produces the highest plateau density and the smallest dissolution radius, leading to the largest accumulated phase shift. These differences are above the typical phase resolution of space-based detectors such as LISA, suggesting that future observations can distinguish between different SIDM annihilation channels and probe the microphysics of dark matter in the vicinity of supermassive black holes.

Our findings highlight that the strength of number changing self-interactions directly affects the inner halo structure, modifying the dynamical friction and consequently influencing the orbital evolution rate of EMRI systems. This establishes a clear connection between the microphysical properties of dark matter and observable gravitational wave signals. Future work may include more detailed modeling of SIDM spike formation, incorporating effects such as black hole spin, eccentric orbits, baryonic feedback, and comparisons with electromagnetic probes like gamma-ray or radio observations. Such efforts will further enhance the prospects of using EMRIs systems as powerful laboratories to study the particle nature of dark matter in extreme astrophysical environments. This study systematically compares phase shifts from different $n \to m$ processes, demonstrating LISA's potential to distinguish SIDM microphysics and opening new avenues for probing dark matter in extreme environments.

Author Contributions: Conceptualization: Y.W.; Methodology: Y.W.; Software: Y.W.; Validation: Y.W.; Formal analysis: Y.W.; Investigation: Y.W., R.T.; Resources: E.L.; Data curation: Y.W.; Writing—original draft preparation: Y.W.; Writing—review and editing: R.T., W.H.; Visualization: Y.W.; Supervision: W.H., E.L.; Project administration: W.H.; Funding acquisition: E.L. All authors have read and agreed to the published version of the manuscript.

Funding: This work was supported by the National Key R&D Program of China (Grant No. 2021YFC2203002).

Data Availability Statement: The original contributions presented in this study are included in the article. Further inquiries can be directed to the corresponding author.

Acknowledgments: First, we thank Enwei Liang and Xin Wu for their valuable opinions. Wen-Biao Han was supported by the CAS Project for Young Scientists in Basic Research (Grant No. YSBR-006).

Conflicts of Interest: The authors declare no conflicts of interest.

References

1. Bullock, J.S.; Boylan-Kolchin, M. Small-Scale Challenges to the ΛCDM Paradigm. *Ann. Rev. Astron. Astrophys.* **2017**, *55*, 343–387. [CrossRef]
2. Tulin, S.; Yu, H.-B. Dark Matter Self-interactions and Small Scale Structure. *Phys. Rep.* **2018**, *730*, 1–57. [CrossRef]
3. Hochberg, Y.; Kuflik, E.; Volansky, T.; Wacker, J.G. Mechanism for Thermal Relic Dark Matter of Strongly Interacting Massive Particles. *Phys. Rev. Lett.* **2014**, *113*, 171301. [CrossRef]
4. Hochberg, Y.; Kuflik, E.; Murayama, H.; Volansky, T.; Wacker, J.G. Model for Thermal Relic Dark Matter of Strongly Interacting Massive Particles. *Phys. Rev. Lett.* **2015**, *115*, 021301. [CrossRef] [PubMed]
5. Gondolo, P.; Silk, J. Dark Matter Annihilation at the Galactic Center. *Phys. Rev. Lett.* **1999**, *83*, 1719. [CrossRef]
6. Shapiro, S.L.; Paschalidis, V. Self-interacting dark matter cusps around massive black holes. *Phys. Rev. D* **2014**, *89*, 023506. [CrossRef]
7. Alvarez, G.; Yu, H.-B. Density spikes near black holes in self-interacting dark matter halos and indirect detection constraints. *Phys. Rev. D* **2021**, *104*, 043013. [CrossRef]
8. Gao, Z.-F.; Li, B.-P.; de Andrade, L.C.G.; Yang, X.-F. On the Theoretical Properties and Experimental Detection of Dark Matter Axions. *Astron. Nachrichten* **2025**, *346*, e70031. [CrossRef]
9. Gao, Z.-F.; Li, B.-P.; de Andrade, L.C.G. Dark photons and tachyonic instability induced by Barbero-Immirzi parameter and axion-torsion transmutation. *Eur. Phys. J. C* **2025**, *85*, 433. [CrossRef]

10. Gao, Z.-F.; Li, B.-P.; de Andrade, L.C.G. Is there a chiral dark dynamo in the universe induced by quantum correction, Nieh–Yan gravity and Barbero–Immirzi field? *arXiv* **2025**, arXiv:2502.04727. [CrossRef]
11. Gao, Z.-F.; Xing, C.-C.; Na, W. The scattering of Dirac spinors in rotating spheroids. *Eur. Phys. J. C* **2020**, *80*, 582. [CrossRef]
12. Gao, Z.-F.; Zhao, X.-J.; Yang, X.-F.; Ma, W.-Q.; Hu, Z.-R. Modified Field Equation With Gauss–Bonnet Gravity. *Astron. Nachrichten* **2025**, *346*, e20250027. [CrossRef]
13. Amaro-Seoane, P.; Gair, J.R.; Freitag, M.; Coleman Miller, M.; Mandel, I.; Cutler, C.J.; Babak, S. Intermediate and Extreme Mass-Ratio Inspirals—Astrophysics, Science Applications and Detection Using LISA. *Class. Quantum Grav.* **2007**, *24*, R113–R169. [CrossRef]
14. Babak, S.; Gair, J.; Sesana, A.; Barausse, E.; Sopuerta, C.F.; Berry, C.P.; Klein, A. Science with the Space-Based Interferometer LISA. V. Extreme Mass-Ratio Inspirals. *Phys. Rev. D* **2017**, *95*, 103012. [CrossRef]
15. Eda, K.; Itoh, Y.; Kuroyanagi, S.; Silk, J. New Probe of Dark-Matter Properties: Gravitational Waves from an Intermediate-Mass Black Hole Embedded in a Dark-Matter Minispike. *Phys. Rev. Lett.* **2013**, *110*, 221101. [CrossRef]
16. Yue, X.; Han, W.-B. Gravitational Waves from Extreme Mass Ratio Inspirals in Dark Matter Spikes: A Numerical Study. *Phys. Rev. D* **2018**, *97*, 064003. [CrossRef]
17. Wang, Y.; Han, W.; Wu, X.; Liang, E. Gravitational wave imprints of dark matter annihilation: Probing halo structures through EMRI signals. *Class. Quantum Grav.* **2025**, *42*, 175007. [CrossRef]
18. Li, B.-P.; Gao, Z.-F.; Ma, W.-Q.; Cheng, Q. Braking index of PSR J1846-0258: A model of magnetic inclination evolution and its gravitational-wave implication. *Front. Astron. Space Sci.* **2025**, *12*, 1625459. [CrossRef]
19. Hochberg, Y.; Kuflik, E.; Volansky, T.; Wacker, J.G. The SIMP Miracle. *arXiv* **2014**, arXiv:1402.5143. [CrossRef]
20. Bernal, N.; Chu, X. Z2 SIMP Dark Matter. *JCAP* **2015**, *1510*, 027.
21. Choi, S.M.; Kim, J.; Ko, P.; Li, J. A multi-component SIMP model with $U(1)X \to Z_2 \times Z_3$. *arXiv* **2021**, arXiv:2103.05956. [CrossRef]
22. Blinnikov, S.I.; Khlopov, M.Y. On possible effects of 'mirror' particles. *Sov. J. Nucl. Phys.* **1982**, *36*, 472.
23. Berezhiani, Z.G.; Dolgov, A.D.; Mohapatra, R.N. Asymmetric inflationary reheating and the nature of mirror universe. *Phys. Lett. B* **1996**, *375*, 26. [CrossRef]
24. Mohapatra, R.N.; Okada, N. Matter-dark matter coincidence and the mirror world. *Phys. Rev. D* **2025**, *111*, 123510. [CrossRef]
25. Mohapatra, R.N.; Nussinov, S. Neutron-Mirror Neutron Oscillation Constraints. *Phys. Lett. B* **2017**, *769*, 247.
26. Ciarcelluti, P.; Wallemacq, S. Cosmological constraints on mirror dark matter. *Int. J. Mod. Phys. D* **2014**, *23*, 1450013.
27. Ciarcelluti, P.; Foot, R. Mirror dark matter and the DAMA/Libra signal. *Phys. Lett. B* **2008**, *679*, 278. [CrossRef]
28. Beylin, V.A.; Bikbaev, T.E.; Khlopov, M.Y.; Mayorov, A.G.; Sopin, D.O. Dark Atoms of Nuclear Interacting Dark Matter. *Universe* **2024**, *10*, 368. [CrossRef]
29. Bertone, G.; Hooper, D.; Silk, J. Particle dark matter: Evidence, candidates and constraints. *Phys. Rept.* **2005**, *405*, 279. [CrossRef]
30. Spergel, D.N.; Steinhardt, P.J. Observational evidence for self-interacting cold dark matter. *Phys. Rev. Lett.* **2000**, *84*, 3760. [CrossRef]
31. Chu, X.; Dekker, A.; Pradler, J. Self-heating dark matter via semi-annihilation. *JCAP* **2019**, *12*, 034.
32. Abazajian, K.N.; Horiuchi, S.; Kaplinghat, M.; Keeley, R.E.; Macias, O. Strong constraints on thermal relic dark matter from Fermi-LAT observations of the Galactic Center. *Phys. Rev. D* **2020**, *102*, 043012. [CrossRef]
33. Kamenetskaia, B.B.; Fujiwara, M.; Ibarra, A.; Toma, T. Dark matter spikes with strongly self-interacting particles. *arXiv* **2025**, arXiv:2506.12642. [CrossRef]
34. Navarro, J.F.; Frenk, C.S.; White, S.D.M. The Structure of Cold Dark Matter Halos. *Astrophys. J.* **1996**, *462*, 563. [CrossRef]
35. Hopman, C.; Alexander, T. The Effect of Mass Segregation on Gravitational Wave Sources near Massive Black Holes. *Astrophys. J.* **2005**, *629*, 362–372. [CrossRef]
36. Barausse, E.; Cardoso, V.; Pani, P. Environmental Effects for Gravitational-Wave Astrophysics. *Phys. Rev. D* **2014**, *89*, 104059. [CrossRef]
37. Linial, I.; Metzger, B.D. Environmental Perturbations on EMRI Evolution in Galactic Nuclei. *Mon. Not. R. Astron. Soc.* **2023**, *520*, 1234–1245.
38. Gnedin, O.Y.; Primack, J.R. Dark Matter Profile in the Galactic Center. *Phys. Rev. Lett.* **2004**, *93*, 061302. [CrossRef] [PubMed]
39. Merritt, D.; Milosavljevic, M.; Verde, L.; Jimenez, R. Dark Matter Spikes and Annihilation Radiation from the Galactic Center. *Astrophys. J.* **2002**, *569*, 51–61. [CrossRef]
40. Peng, X.; Chen, Y. Impact of Gas and Stellar Background on EMRI Gravitational Waveforms. *Astrophys. J. Lett.* **2025**, *940*, L12.
41. Eda, K.; Itoh, Y.; Kuroyanagi, S.; Silk, J. Gravitational waves as a probe of dark matter minispikes. *Phys. Rev. D* **2015**, *91*, 044045. [CrossRef]
42. Peters, P.C.; Mathews, J. Gravitational radiation from point masses in a Keplerian orbit. *Phys. Rev.* **1963**, *131*, 435. [CrossRef]
43. Chandrasekhar, S. Dynamical friction. I. General considerations: The coefficient of dynamical friction. *Astrophys. J.* **1943**, *97*, 255. [CrossRef]

44. Barack, L.; Cutler, C. LISA Capture Sources: Approximate Waveforms, Signal-to-Noise Ratios, and Parameter Estimation Accuracy. *Phys. Rev. D* **2004**, *69*, 082005. [CrossRef]
45. Bonga, B.; Yang, H.; Hughes, S.A. Tidal resonance in extreme mass-ratio inspirals. *Phys. Rev. Lett.* **2019**, *123*, 101103. [CrossRef] [PubMed]